Global spectral analysis of three-time level integration schemes: Focusing phenomenon

Tapan Sengupta, Pierre Sagaut, Aditi Sengupta, Kumar Saurabh

Global Spectral Analysis of Three–time Level Integration Schemes: Focusing Phenomenon

Tapan K. Sengupta,[1], Pierre Sagaut**, Aditi Sengupta* and Kumar Saurabh

High Performance Computing Laboratory, Department of Aerospace Engineering, I. I. T. Kanpur, Kanpur 208016, India, e-mail: kumar.saurabh@gmail.com
**currently at Dept. of Engineering, Univ. of Cambridge, U. K. e-mail: dolaaditi@gmail.com,*
***Professor, Aix-Marseille Universit, Marseille Laboratoire de Mcanique, Modlisation et Procds Propres, France, e-mail: pierre.sagaut@univ-amu.fr*

Abstract

Here, we explain the phenomenon of focusing using the numerical properties of space–time discretization methods involving second-order Adams–Bashforth (AB2) method for the solution of one–dimensional (1D) convection equation. It has been established that solving 1D convection equation by three–time level method invokes a numerical or spurious mode, apart from the physical mode (as explained in Global spectral analysis of multi–level time integration schemes: Numerical properties for error analysis T. K. Sengupta *et al.*, Applied Mathematics and Computation, **304**, 41-57 (2017)). Here, the long elusive problem of focusing (considered as a problem of non-linear numerical aspect), is shown due to a linear mechanism. The focusing is shown for a wave–packet propagating in a non-periodic domain by a three–time level method. Long time integration shows the physical mode to cause focusing, which shows up as spectacular growth of error–packet(s) at discrete location(s), where the dominant wavenumber (k) depends only on the CFL number (N_c), for the space–time discretization method. The length scale of growing error is independent of wavenumber of the input signal. It is also established that focusing is related to numerical absolute instability, for which the numerical group velocity (V_{gN1}) of the physical mode is zero. However, interestingly, when a compact filter is used, the focusing phenomenon is converted from absolute to convective numerical instability. This brings new insight and satisfactory explanation of focusing and its dependence on the choice of numerical methods and use of filter. As a demonstration of the focusing phenomenon for AB2 method, we use it with a well known combined compact differencing scheme to solve Navier–Stokes equation in a square lid driven cavity for a super-critical post–Hopf bifurcation Reynolds number of 10000 (based on the side of the cavity and the constant lid velocity). Contrary to the well-established solution with polygonal vortices in the literature, here the solution breaks down after a finite time due to focusing.

Keywords: Three–time level integration method, Global spectral analysis, Focusing phenomenon, Absolute instability, One–dimensional filtering, Convective instability,

[1]Corresponding author; e-mail: tksen@iitk.ac.in (Tapan K. Sengupta)

DNS.

1. Introduction

Space–time discretization methods have been studied in extensively depth in recent times by the authors' group in [18, 20, 24] by global spectral analysis (GSA). For a governing equation with first derivative with respect to time, analysis of numerical amplification in the spectral plane (as described in [18]), reveals the necessity of using two–time level methods, otherwise spurious numerical mode(s) appear. This aspect has been described in [18] for mid-point leapfrog method. In [26], this has been shown for AB2 [1] and second-order extrapolation in time (EXT2) methods of time integration used with different explicit and Hermitian spatial discretization methods. There appears to be some misconception about the existence and harmful effects of the numerical mode for AB2 method, as it is used in many works, discussed in [26]. In the context of evaluating space–time discretization methods together, 1D convection equation is used extensively in [16, 18, 21, 31, 32, 33] to quantify the main sources of numerical error. For this, the model equation in Cauchy framework is,

$$\frac{\partial u}{\partial t} = -c\frac{\partial u}{\partial x}; \quad \text{for } c > 0, \quad -\infty < x < +\infty \tag{1}$$

with suitable initial condition provided: $u(x,0) = f(x)$ which provides analytical solution for any x and t, given by $f(x-ct)$. The comprehensive GSA tool developed in [18, 21, 22] for non-periodic, parabolic and hyperbolic PDEs for the full domain enables one to quantify the numerical properties of spatio–temporal discretization methods. This is different from that described in [5, 15], which follows the von Neumann error dynamics analysis that assumes the signal and error to follow the same governing equation for systems governed by linear partial differential equations. Actual error dynamics for 1D convection equation has been described in [18, 21] which shows that additional forcing appears due to various sources of numerical error due to dissipation and dispersion. The GSA defined in Fourier spectral plane for space, is different from von Neumann analysis to study error dynamics, as is explained in [26]. One defines error here as, $e(x,t) = u(x,t) - u_N(x,t)$, with u_N, the numerically computed solution expressed by the hybrid representation at the j^{th} node (x_j) of a uniform grid with spacing h by,

$$u_N(x_j, t^n) = \int U_j(kh, t^n)\, e^{ikx_j} dk$$

where current time is indicated by t_n. In the integrand, U_j represents the bi-lateral Laplace transform and the integration range is determined by the Nyquist limit of $\pm\pi/h$. We have defined the numerical amplification factor at the j^{th} node by, $G_j(kh, N_c) = U_j(k, t^{n+1})/U_j(k, t^n)$ to characterize numerical stability/ instability for the combined space–time discretization methods, where N_c is the CFL number defined by $c\Delta t/h$, with Δt as the time step used. This complex quantity is furthermore denoted as, $G_j = G_{rj} + iG_{ij}$, with the subscripts, r and i, denoting the real and imaginary part, respectively.

The values of G_{rj} and G_{ij} determine the numerical phase shift caused per time step (β_j) and is responsible for the numerical solution of Eq. (1) propagating from left to right with a numerical phase speed (c_N), which can deviate from the physical phase speed c. Note that the numerical phase shift is given by, $\tan\beta_j = -G_{ij}/G_{rj}$, which need not be equal to the physical phase shift given by, $c\Delta t$. The numerical phase shift is alternatively obtained from $c_N\Delta t$. These relations help us relating c with c_N. For the same reason, the group velocity [4] of the numerical method (V_{gN}) will be different from the physical group velocity (for Eq. (1), the physical group velocity is also equal to c, which makes the governing equation non-dispersive). Furthermore, as G_{rj} and G_{ij} are functions of kh and N_c, it is evident that c_N becomes a function of kh and N_c. Thus for the original non-dissipative, non-dispersive equation, the numerical solution will be dissipative (unstable) depending upon $|G_j|$ greater (lesser) than one.

The numerical phase speed and numerical group velocity for Eq. (1) can be obtained from the discretized form of the equation, as shown in [26]. The numerical phase speed (c_N) is obtained from, $kc_N = \beta_j/\Delta t$, with the correct numerical dispersion relation obtained by considering space and time discretizations given in [18, 21], $\omega_N = kc_N$. This provided the numerical group velocity as, $V_{gN} = \frac{d\omega_N}{dk} = c_N + \frac{dc_N}{dk}$. For three–time level methods, the discretized governing equation will give a quadratic for G_j, as described in [18]. This in turn will produce two values of the phase shift, giving rise to two values of $(c_N)_{1,2}$ and numerical group velocity as, $V_{gN1,2}$. The process followed for three–time level methods is identical to that used for two–time level methods.

In many physical applications, numerical solution with multi–level time integration methods are seen to blow up suddenly after producing results for long computational time, and this has not been satisfactorily explained yet. Such spontaneous growth of error was often attributed to nonlinear numerical instability by [3, 11, 17, 30]. Here, we show that the main issue is that the error dynamics based on von Neumann analysis is inadequate to explain even the linear instability. The situation has changed since the appearance of correct numerical dispersion relation in [18, 20, 21]. This inadequacy can be attributed to the dispersion relation adopted in von Neumann analysis ($\omega_N = k_{eq}c$) in [5, 10, 15], as explained by [26]. Aspects of dispersive and non-dispersive wave solutions have been discussed earlier in [10, 16, 31, 32] without the appropriate dispersion relation.

The central assumption in classical analysis is that the error and the signal follow the same equation and for Eq. (1), this leads ostensibly to the error propagation equation

$$\frac{\partial e}{\partial t} + c\frac{\partial e}{\partial x} = 0, \quad \text{for } \; c > 0; \;\; \text{and} \;\; -\infty < x < +\infty \tag{2}$$

In contrast, the authors in [21] have provided the more appropriate error propagation equation for two–time level methods, based on the correct numerical dispersion relation ($\omega_N = kc_N$), for Eq. (1) to be governed by,

$$\frac{\partial e}{\partial t} + c\frac{\partial e}{\partial x} = -c\left[1 - \frac{c_N}{c}\right]\frac{\partial \bar{u}_N}{\partial x} - \int \frac{V_{gN} - c_N}{k}\left[\int_0^k ik' A_0 \, [|G|]^{t/\Delta t} \, e^{ik'(x - c_N t)} dk'\right] dk$$

$$-\int \frac{\text{Ln } |G|}{\Delta t} A_0 \, [|G|]^{t/\Delta t} \, e^{ik(x-c_N t)} \, dk, \tag{3}$$

with initial condition given by, $u(x,0) = \int A_0(k) e^{ikx} dk$. Here for the ease of representation, we have omitted the subscript from G with the understanding that one is focusing upon the j^{th} node. Physically, the phase speed is the speed with which the phase at any point moves, while the group velocity is related to energy propagation speed [18, 31] and for a non-dispersive system as Eq. (1), these two are the same. Here, for any arbitrary numerical method, $c_N \neq V_{gN} \neq c$ [18, 26]. The error dynamics, Eq. (3), for Eq. (1) holds for any discrete method analyzed for space–time discretization together. The evolution of the error equation is expressed as a forced excitation problem. The terms on the right hand side of Eq. (3) arises: (i) due to phase error given by the first term; (ii) the dispersion error consisting of the first and second terms and (iii) the last term on right hand side of Eq. (3) is the dissipation error and comes into play whenever $|G| \neq 1$.

Adoption of von Neumann's theory of computing with Fourier analysis cannot explain many situations, which prompted the author in [33] to state that "through Fourier analysis, one can evaluate the phase and amplitude error of a given method as a function of the wavenumber. However, this information can be difficult to interpret".

The GSA reveals the features of error to help identify the limits of computational parameters for which the error is minimal. These numerical properties have been obtained for some representative two–time level methods in [18] and for AB2 scheme in [26], where the correct error propagation equation is quoted for arbitrary space–time discretization methods by Eq. (3) above for the model Eq. (1).

While discussing the linear focusing mechanism for dispersive and non-dispersive wave problem in [2], the authors summarized the state of art with respect to two–time level methods used with compact schemes. In the reference, for the first time, a linear focusing mechanism for the wave–packet propagation was explained for a non-periodic problem. Focusing for compact scheme was noted for three different scenarios: (i) it can be associated with discontinuity in the numerical solution; (ii) it can be observed near boundary nodes due to poor performance of boundary closure schemes for basic compact schemes and (iii) it has strong dependence on the chosen methods of discretization. The phenomena studied were due to the non-physical nature of boundary closure schemes used in all compact schemes with two–time level methods. Here, we discuss about three–time level methods, used with different explicit and implicit spatial discretization methods.

It is postulated by various researchers that violent instability appears in a short span of time (as compared to total computing time) by a nonlinear mechanism previously documented in [3, 11, 17, 30]. Briggs *et al.* [3] proposed a mechanism by which the error is focused at one point in the computational domain for the inviscid Burgers' equation, solved as a periodic nonlinear problem. This governing equation was quasi-linearized and a three–time level leapfrog method has been used for time advancement, along with second–order central difference (CD2) scheme. It was specifically noted that *noise can localize on spatial grid and cause finite amplitude instability thresholds to be exceeded at distinct locations.* Other

references on focusing also demonstrated its existence by using three–time level methods such as that reported in [11, 30], where mid–point leapfrog method was used. Sloan and Mitchell [30] explained the phenomenon of focusing by describing the Fourier side–band instability for amplitude modulation. The implication from this observation is equivalent to stating that error–packets develop in the spatial grid.

The paper is formatted in the following manner. In the next section, the dispersion and amplification properties of some three–time level methods shown in [26] are revisited along with some new methods, to emphasize centrality of GSA in explaining focusing of numerical solution. The importance of GSA is furthermore emphasized by explaining the phenomenon of focusing and its classification in section 3. In section 4, we solve Navier–Stokes equation for flow inside a square lid driven cavity (LDC) at a high Reynolds number, for which the flow is unsteady [29], by AB2 time integration method along with a high order combined compact difference scheme to show focusing, which has produced accurate results with four-stage, fourth-order Runge–Kutta method [23, 28]. We summarize the paper in section 5, along with some specific conclusions regarding focusing and the means to avoid the phenomenon.

2. Dispersion Properties explained by GSA of Three–time Level Methods

In [26] we have noted that AB2 method suffers due to presence of numerical mode, which introduces error and in some cases produces highly erroneous results. Present research focuses on AB2 time integration method, as it continues to be used for DNS/ LES of flows by solving Navier–Stokes equation [13, 14] and other references cited in [26], using many methods for spatial discretization.

In [26] one notes the numerical solution of Eq. (1) by AB2–CD2 method for the choice of $kh = 0.3$, $N_c = 0.1$ and $c = 1$, to suffer mainly from dispersion error, while the error due to numerical amplification factor is small, while solving Eq. (1) for an aeroacoustic benchmark problem in a domain $-600 \leq x \leq 1200$. The initial condition is given by $u(x;0) = [2+\cos(kx)]e^{[-(\ln 2)(x/10)^2]}$, with $k = 1.7$ [9]. In Fig. 1 on the right hand side frames, we show the solution for this kh and N_c, at $t = 380$, 400 and 420. The solutions show dispersion, in terms of location of the packet, with respect to the exact solution plotted together. However, it is not always true that the physical mode will always suffer negligible dissipation error for the solution of Eq. (1). In reporting the results here, we have used $c = 1$ for Figs. 1 and 3 and for the rest of the results in Figs. 4 to 8, we have used $c = 0.5$.

For three–time level methods, one boot-straps the solution from $t = 0$ to $t = \Delta t$. With these solutions at successive time steps, one starts using three–time level methods. If the initial solution has amplitude given by $A_0(k)$, then following the two–time level method, one has the amplitude given by $A_1(kh, N_c) = A_0(k)G_E(kh, N_c)$, as described in [26]. After the application of three–time level method, this amplitude (A_1) splits into A_1G_1M and A_1G_2N. Thus, M and N are the spectral weights by which the solution at $t = \Delta t$ splits itself into physical and numerical modes.

In Fig. 2a, we plot the numerical amplification rates for the physical mode ($|G_1||M|$) of AB2–CD2 and EXT2–CD2 methods. The dissipation error is small for $kh = 0.3$ and $N_c = 0.1$,

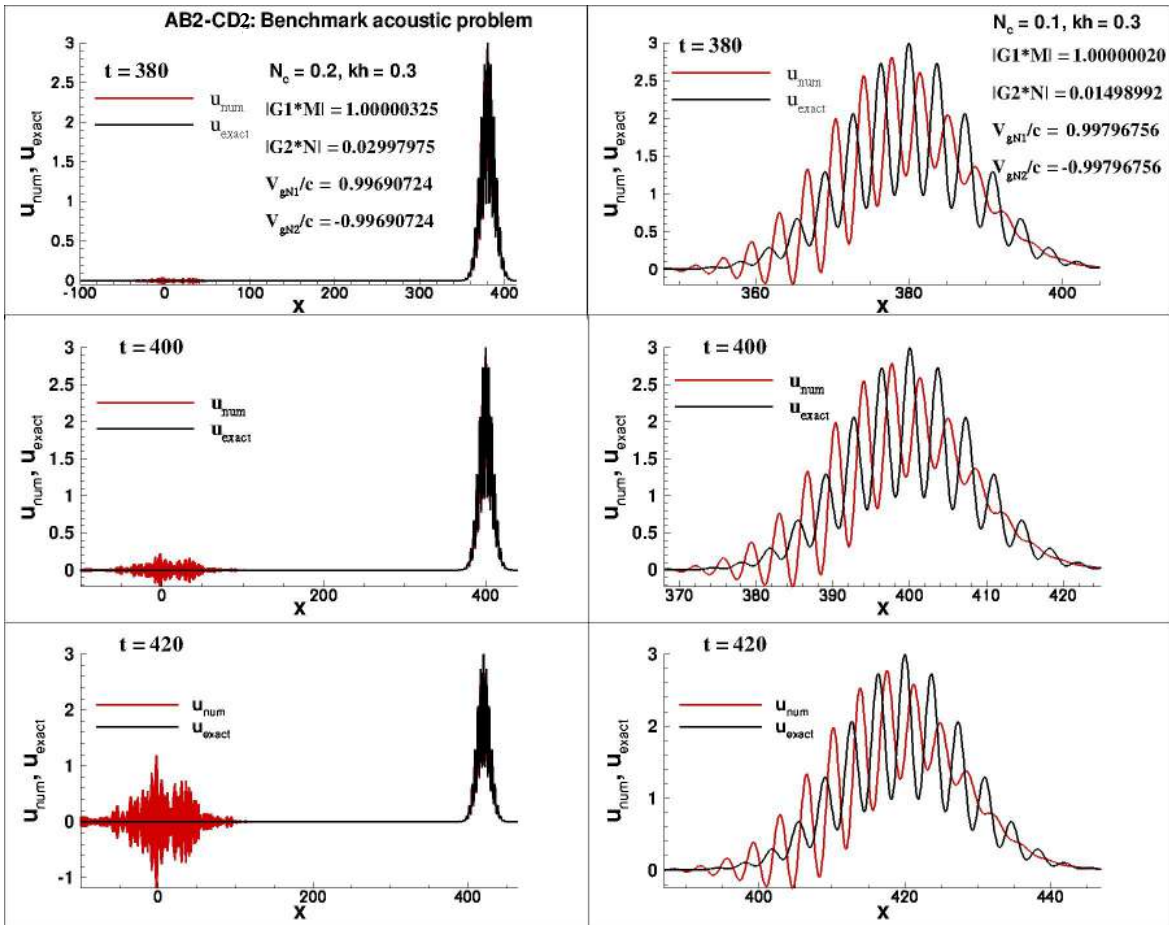

Figure 1: Demonstration of focusing phenomenon for AB2–CD2 method by solving Eq. (1) for the CAA benchmark problem [9] with $kh = 0.3$, $N_c = 0.2$ and $c = 1$ on the left frames and $N_c = 0.1$ for the results on the right hand side frames. Solutions are shown at $t = 380$, 400 and 420. Demonstration of focusing is via the additional error growing near $x = 0$ without convecting.

as the physical mode is mildly unstable ($|G_1||M| = 1.00000020$) for AB2–CD2 method. The numerical mode accounts for about 1.498% of the signal and transmits it upstream. For the value of $N_c = 0.1$, the maximum growth occurs for $kh = \pi/2$, given by $|G_1||M| = 1.00001$, as noted from Fig. 2a. Also for $kh = \pi/2$, $V_{gN1} = 0$ for all CFL numbers, as shown in Fig. 2b, where V_{gN1}/c and V_{gN2}/c are plotted in (kh, N_c) plane for AB2–CD2 method. Zero numerical group velocity for $kh = \pi/2$ for AB2–CD2 method implies that error component with this length scale ($kh = \pi/2$) will be stationary and such solution with $|G_1||M| > 1$ has been termed as absolute instability, due to the inability of the error component to convect [6]. Its cumulative effects, as the computation advanced for long times, cause catastrophic failure of the solution. To understand this, in the left column of Fig. 1, we show the computed solution for the same wave–packet with increased $N_c = 0.2$. For this higher $N_c = 0.2$ with $kh = 0.3$, one notices mild increase in the value of the amplification factor for the physical mode to $|G_1||M| = 1.00000325$ and one would expect that the result would not be greatly different from that shown for $N_c = 0.1$. However, the computed solution shown in Fig. 1 for $N_c = 0.2$, indicates a secondary site of error growth (around $x = 0$, where the initial solution

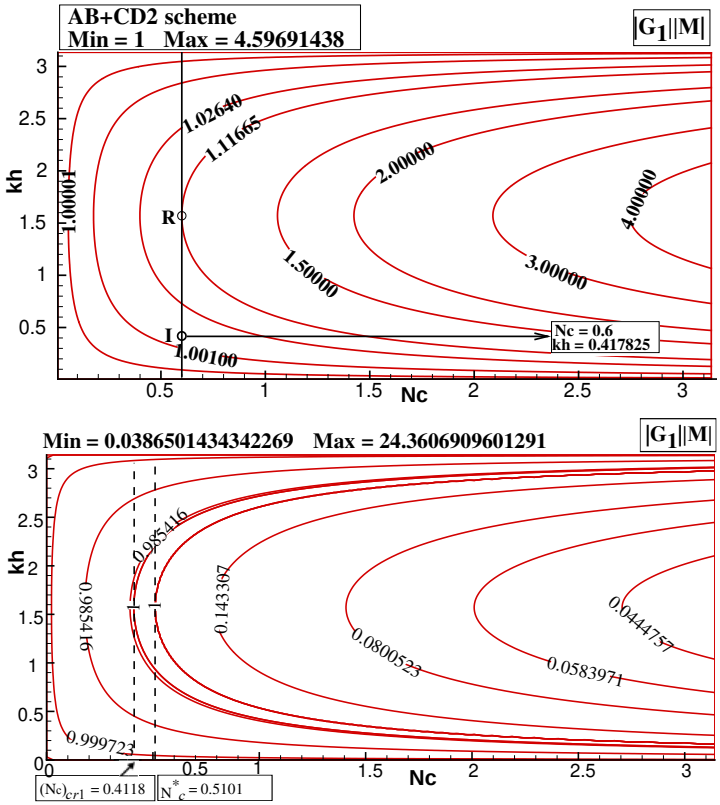

Figure 2a: Numerical amplification rate of physical mode for AB2–CD2 method (top) and EXT2–CD2 method (bottom) for the solution of Eq. (1). Note the points R and I for AB2–CD2 method, which will be used for discussing focusing in Figure 4. For the EXT2–CD2 method, note the existence of multiple critical CFL numbers.

had maximum variation) in the frame shown at $t = 380$. This is due to growth of round–off error, which is present at all resolved length scales. This patch of error is seen to grow rapidly in Fig. 1, when time increases marginally from 400 to 430. This error growth corresponds to the maximum growth rate noted in Fig. 2a, for $N_c = 0.2$ and $kh = \pi/2$ as $|G_1||M| \approx 1.001$. This maximum growth rate is significantly higher than that noted for $N_c = 0.1$. This causes growth of the error and is associated with space-time discretization methods which show zero numerical group velocity and q-wave phenomenon [19] for the specific range of N_c, for which one notices $|G_1||M| > 1$ for some resolved kh. After a long-time of integration, the cumulative growth of error would lead to catastrophic breakdown of solution. In Fig. 1, such growth was not visible for $N_c = 0.1$ up to $t = 600$ (as shown in [26]), while for $N_c = 0.2$ one can see perceptible error growth by $t = 420$, and if it is computed for a little longer, then the solution breaks down. Essentially focusing is noted for a particular higher CFL number, for which there is some length scale, which has zero numerical group velocity and for which the numerical amplification factor indicates numerical instability.

Above discussion also indicates that increasing CFL number can lead to focusing of error. To explain this, we compute another case with $N_c = 0.2$ for EXT2–CD2 method, for which we noted excellent match between computed and exact solutions in [26] for the CAA benchmark

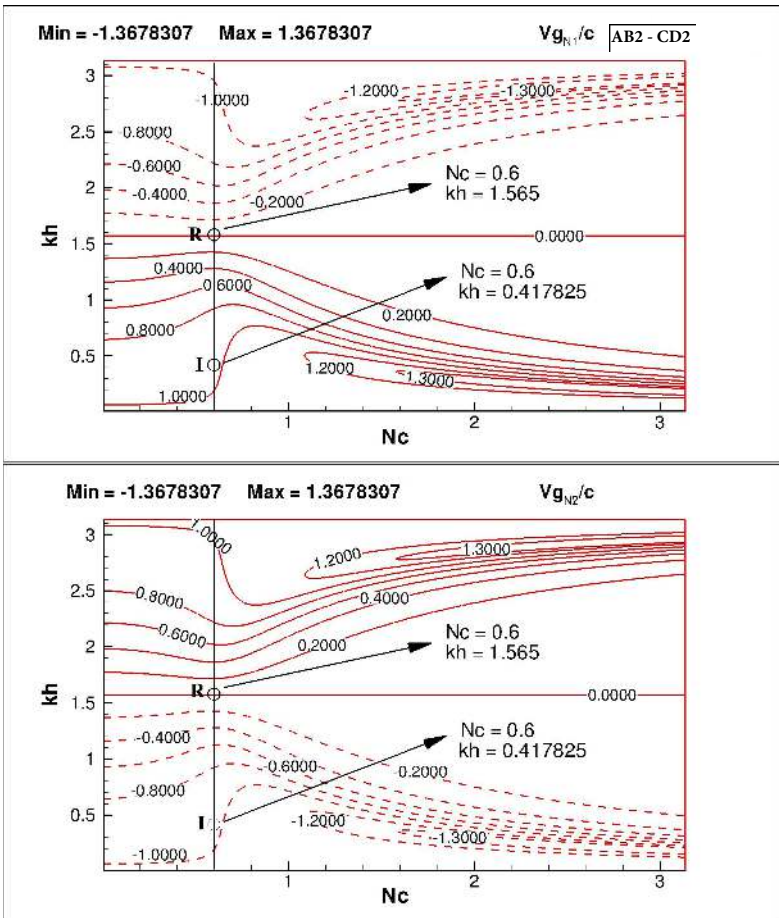

Figure 2b: Numerical group velocity for the physical and numerical modes for AB2–CD2 method for the solution of Eq. (1). Note the point I corresponds to input signal to be used in Fig. 4. The response will correspond to point R, which also has zero numerical group velocity.

problem [9] with $kh = 0.3$ and $N_c = 0.1$ up to $t = 1000$, as also shown in the right hand side frames of Fig. 3. For the case computed with $N_c = 0.2$, results are shown in the left frames of Fig. 3. From the amplification property shown in Fig. 2a, one notices the center of the packet to move upstream, which appears as a large dispersion error. This method also displays q-waves for $kh > \pi/2$, which is not dependent on N_c. However, for $kh = \pi/2$, the method becomes unstable and leads to focusing for $0.4118 \leq N_c \leq 0.5101$, a range where $|G_1||M| > 1$. Such focusing will be intense as the maximum growth rate is very high in this range of CFL numbers, as noted from Fig. 2a, with maximum growth rate crossing over 24. For the choice of $N_c = 0.2$, there is no likelihood of focusing, which is also apparent from Fig. 3. At the same time dispersion error is prominent, while we noted very accurate results for $N_c = 0.1$ in [26] and here in Fig. 3.

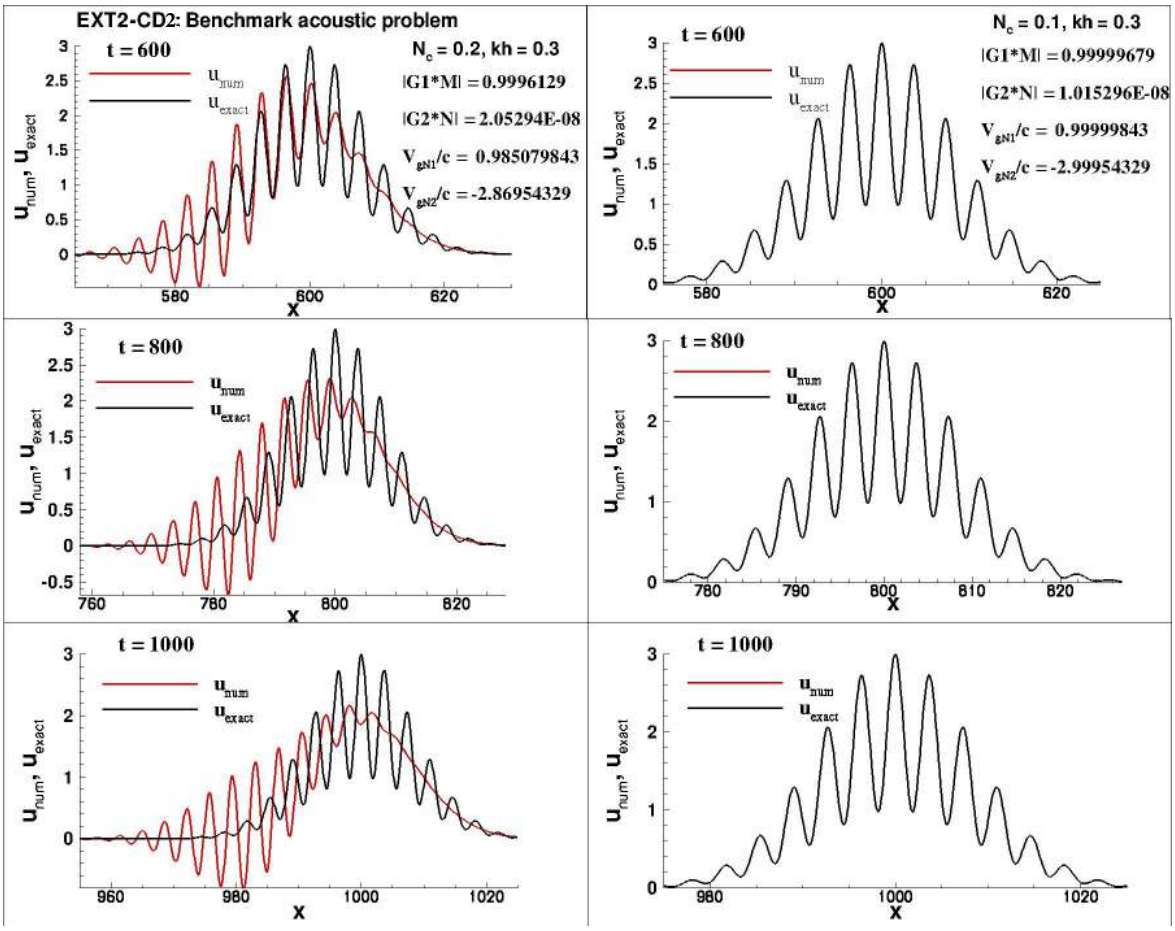

Figure 3: Demonstration of solution for EXT2–CD2 method for Eq. (1) for the CAA benchmark problem [9] ($c = 1$) with $kh = 0.3$, $N_c = 0.1$ results shown in the right column. The solutions for $N_c = 0.2$ are as shown in the left column, which show significant dispersion error at $t = 600$, 800 and 1000, without any symptoms of focusing.

3. Focusing of Error for AB2–Scheme for 1D Convection Equation

Next, we discuss about AB2 time integration scheme to show how focusing is caused by the instability of the physical mode itself, in the linear framework for both explicit central spatial schemes and two Hermitian spatial discretizations. If the explicit spatial discretization scheme is strongly upwinded, as in the case of AB2–UD3 scheme, the same linear mechanism will come into play through the amplification of either the physical mode or the numerical mode (results not shown here). The details of third order upwind scheme, UD3, can be seen in [12, 18, 25].

To explain focusing, we revisit the problem in Eq. (1), with an initial condition of the monochromatic signal convoluted by a Gaussian envelope given by

$$u(x, 0) = e^{-\alpha(x-x_0)^2} \sin(k_0 x) \tag{4}$$

The parameters chosen here are: $\alpha = 0.01, x_0 = 0$ and $k_0 = 20$, with number of points in the computational domain indicated later. The first time step is obtained by Euler integration scheme. Four different spatial schemes with AB2 method have been analyzed and the values of N_c and k_0h are chosen in a way, such that the effects of focusing due to the choice of numerical method are clearly demonstrated. For AB2–CD2 method, $N_c = 0.6$ and $k_0h = 0.417825$ (this point is marked in Fig. 2a as I) are chosen for the periodic problem and results are shown in Fig. 4. In Figs. 4 to 8, the sharp spike near the origin of the plotted spectrum, represents the input signal given by the initial condition of Eq. (4). The periodic problem has been solved to avoid any additional issues arising out of reflections from the boundaries. It is important that the input wave is resolved sufficiently in the k-plane. This is the reason that in the domain, from 0 to 3000 we have taken uniformly spaced points with $h = 0.02089125$. In the top frame of the figure, the initial condition is displayed for the representative range of x in the center of the domain where the function is non-zero. Its spectrum at $t = 0$ can be noted in the bottom frame of Fig. 4 as the bottom-most curve in the ensemble. The bottom frame shows the spectrum of the computed solutions at different time steps. The variation with time of the spectrum is indicated by successive curves displaying growing peaks. The numerical solution shown in Fig. 4b at $t = 520\Delta t$, displays formation of wave-packets with ever-growing amplitude in time. For the initial condition taken in solving Eq. (1), the response is noted to focus around $kh = 1.565$, as shown in Fig. 4c, where the Fourier transform of the numerical solution is shown for increasing time instants to grow monotonically due to zero group velocity of this spectral component, shown all the way up to $t = 520\Delta t$.

In Fig. 2a for $N_c = 0.6$, split amplification rate $|G_1||M|$ is maximum for the physical mode for $k_0h = 1.565$ indicated by R, while the input signal is marked as I. It is noted that as N_c reduces, maximum value of $|G_1||M|$ also reduces. This strengthens the argument that one should remain close to origin, i.e., $N_c \to 0$, as the maximum $|G_1||M|$ continuously reduces with reduction in N_c. If additional filtering is applied on the numerical solution (as explained later), then this will delay focusing to much later times or not at all. The initial packet formation noted in Fig. 4b is due to the fact that the side–bands of $k_0h = 1.565$ are also unstable and have similar amplitudes, which have their origin in round–off error, acting like band–limited white noise. Such neighbouring signals with higher growth rates dominate and form wave–packets. This provides the initial algebraic growth due to mutual reinforcement of neighbouring wavenumbers and is noted in the physical plane. Thus, the focusing phenomenon causes localization in k–space, while in physical space the numerical solution displays wave–packets at early stages (as we noted in Fig. 1 for $N_c = 0.2$). In a few time steps after $t = 520\Delta t$, the solution of Fig. 4 blows up. The side–band of $k_0h = 1.565$ tapers off to lower growth rate, decided upon by the numerical properties obtained by GSA. Thus computing with higher precision, occurrence of focusing will be delayed, yet focusing will always occur for $N_c \geq (N_c)_{cr1}$ (as noted in Fig. 2a). One also notices that the focused signal at the center does not propagate, as the central kh has zero group velocity, according to Fig. 2b. This has also been noted for other cases reported below, except when stated otherwise.

Similarly, AB2–CD4 method is used for the same problem and the results are reported in Fig. 5. As we have used the same domain with same initial condition, the response of the

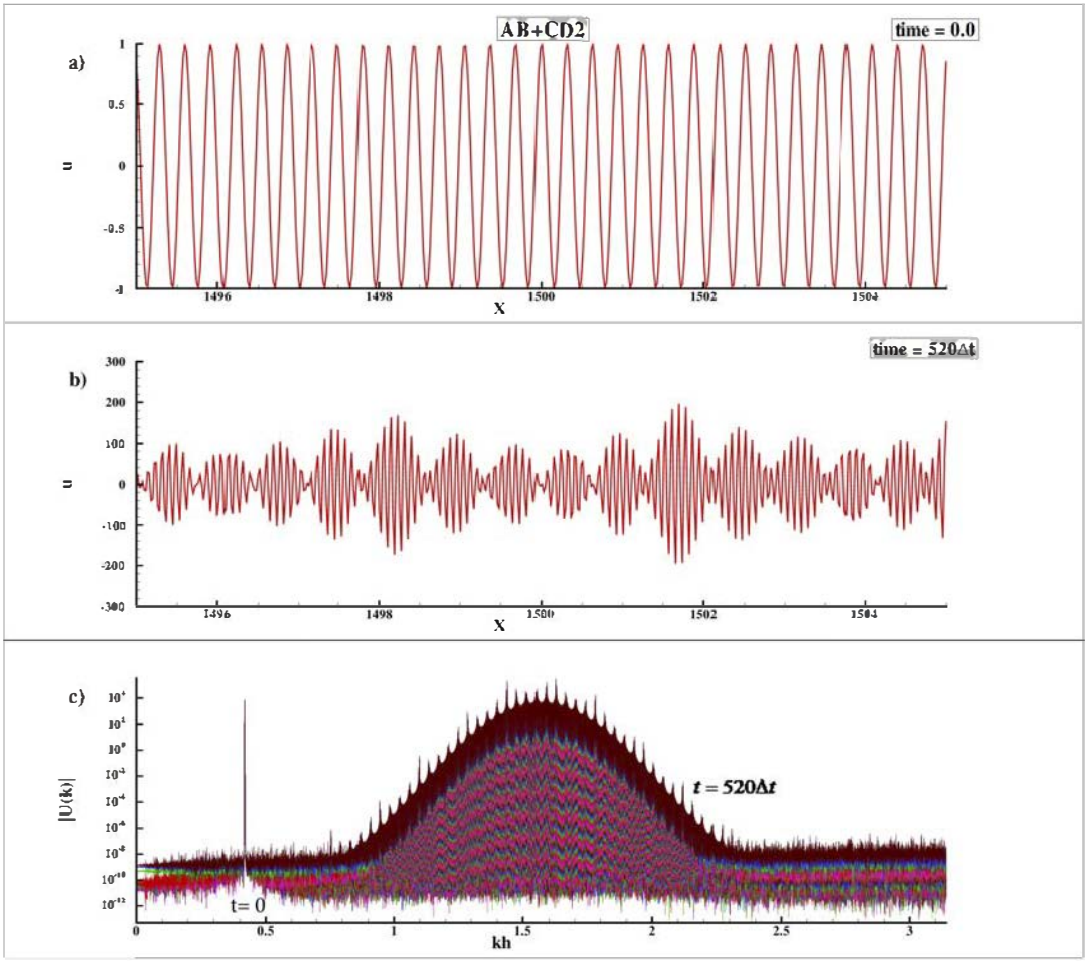

Figure 4: Demonstration of focusing phenomenon for AB2–CD2 method by solving Eq. (1) for $N_c = 0.6$; $k_0h = 0.417825$ and $h = 0.02089125$. (a) Initial signal shown centered at $x_0 = 1500$. (b) Signal at $t = 520\Delta t$, with focusing affecting the entire domain. (c) Demonstration of focusing as a function of kh with time as parameter, increasing from $t = 0$ (bottom line) to $t = 520\Delta t$ (the top most line).

system will be dictated by the properties shown in [26]. In this case, for the same value of $N_c = 0.6$, one notices more violent instability as compared to the CD2 scheme results shown in Fig. 4. Also, apart from having higher growth rates, it is also noted to occur at higher wavenumber, $kh = 1.8$ for which $V_{gN1} = 0$. The physical plane solution is on the verge of breakdown at an earlier time shown at $t = 140\Delta t$ in Fig. 5a. Corresponding spectral plane data are shown in Fig. 5b. Once again, the scale selection of error is based on the maximum growth rate for fixed N_c value starting from the side–band of the chosen wave–packet at $t = 0$. The maximum growth rate components will mutually interfere with its immediate neighbouring wavenumbers and form response wave–packet at $kh = 1.8$ and is readily evident from Fig. 5b.

Hermitian spatial discretization, OUCS3 [22] and Lele's 10^{th}–order schemes, in conjunction with AB2 and variable–time step predictor–corrector (VTSPC) time integration methods [7, 8], respectively, have been analyzed next. In Fig. 6, results for AB2–OUCS3 method are

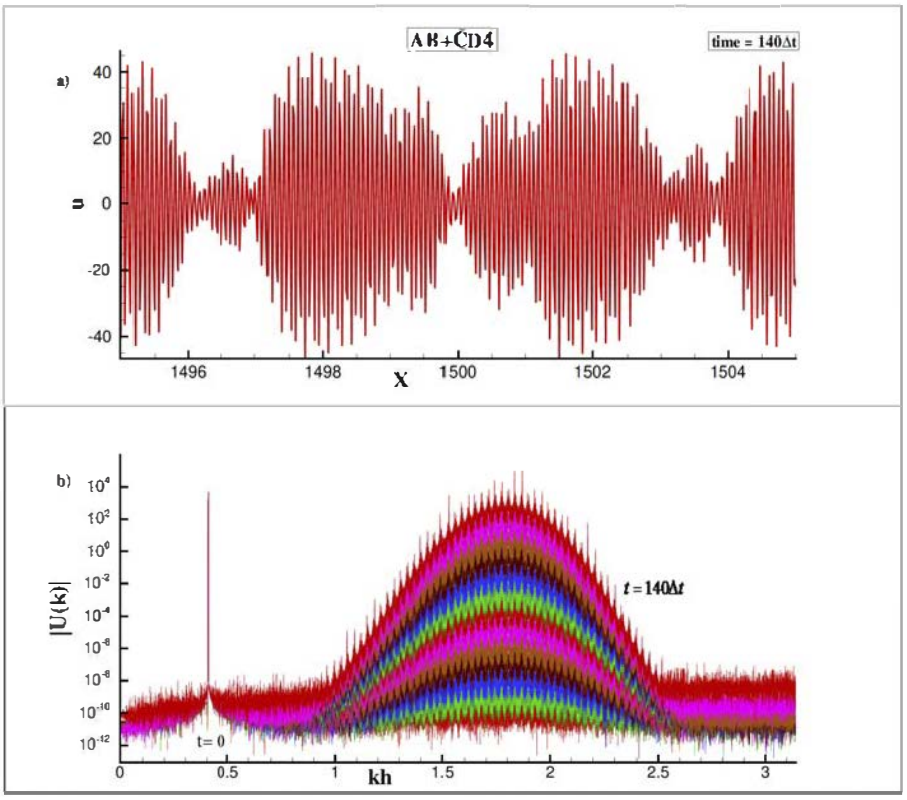

Figure 5: Demonstration of focusing phenomenon for AB2–CD4 method by solving Eq. (1) with the same initial solution used in Fig. 4; (a) Solution at $t = 140\Delta t$ indicate focusing, that affects the entire domain. (b) Demonstration of focusing by plotting $U(k)$ as a function of kh, with time as parameter increasing from bottom ($t = 0$) to the top line ($t = 140\Delta t$).

shown for the solution of Eq. (1), in an identical domain using same initial condition as the ones used for Figs. 4 and 5. Here the input signal has $k_0 h = 0.406710$, while N_c has the same value of 0.6. Corresponding numerical stability properties have been shown in [26], which help one identify the property of the response shown in Fig. 6. The computed solution in physical space, as shown in Fig. 6a, shows focusing to occur at even higher wavenumbers for this method, as noted in Fig. 6b. This wavenumber is also higher than that of the AB2–CD4 method shown in Fig. 5.

In Fig. 6b, one observes response of the system focusing at $kh = 2.4$, which is consistent with the point R marked in Fig. 6c. These property chart has been obtained and shown in [26]. The response field remains frozen in space, with amplitude growing in time, due to the fact that the group velocity corresponding to $kh = 2.4$ is zero [26]. Such a growth, only with time and with the error localized, has been identified in [6] as absolute instability. This attribute has been already noted in Figs. 4 and 5 for AB2–CD2 and AB2–CD4 methods, for which the focused error does not convect due to $V_{gN1} = 0$.

In Fig. 7 we display the solution of Eq. (1) for the case of VTSPC time integration method used with Lele's 10^{th}–order spatial discretization scheme. Qualitatively, one observes a behaviour similar to that shown in Fig. 6. In this case, the input signal propagation is studied

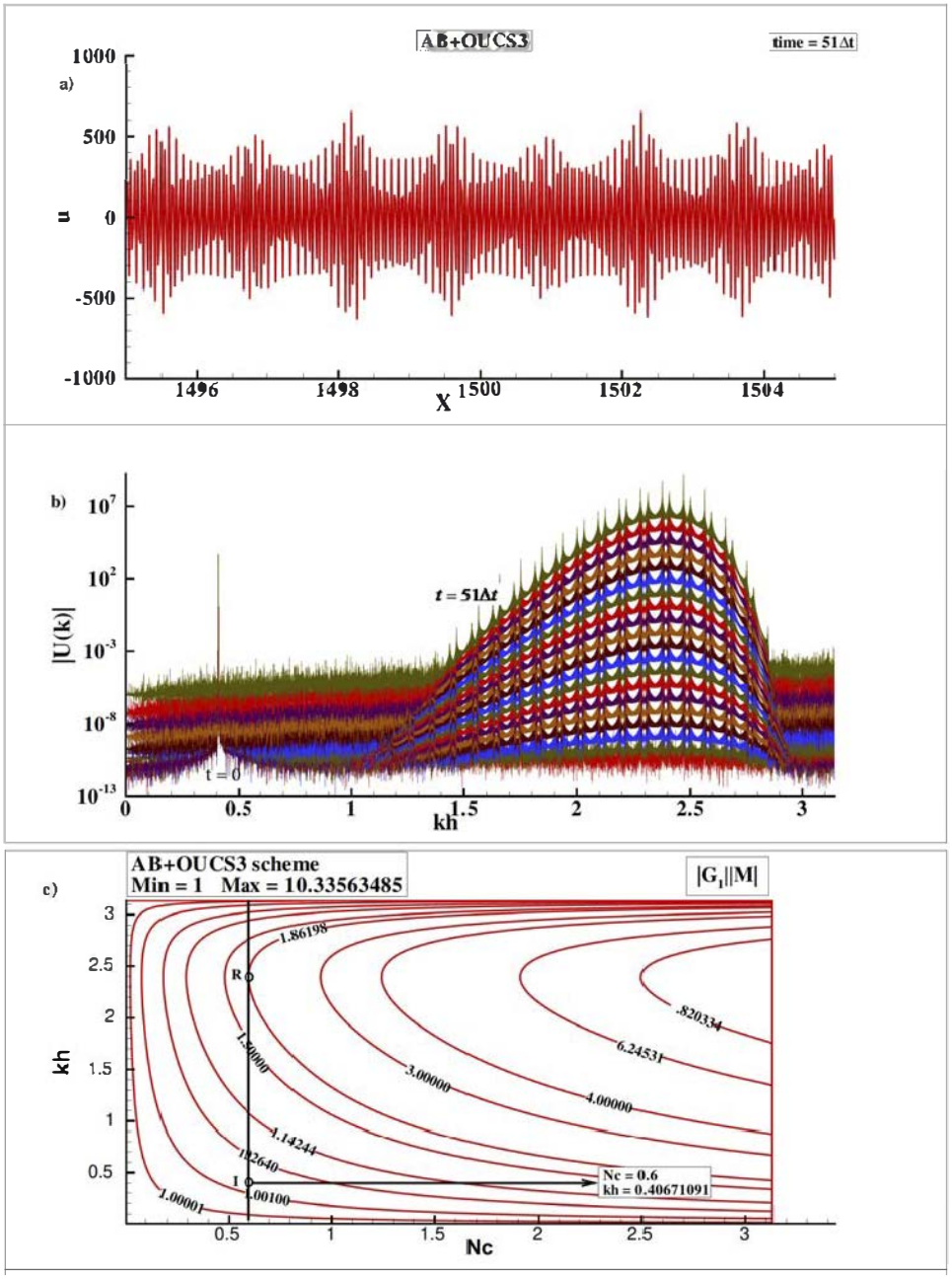

Figure 6: Solution of Eq. (1) by AB2–OUCS3 method with $k_0h = 0.406710$ and $N_c = 0.6$; (a) Signal at $t = 51\Delta t$. (b) Demonstration of focusing by plotting time evolution of $U(k)$ as a function of kh. (c) The numerical growth rate of the physical mode $|G_1||M|$ in the (N_c, kh)-plane with the input signal marked as I and the focused output identified by R.

for $N_c = 0.6$ and $k_0h = 0.1723782$, as shown in Fig. 7a. For the VTSPC method, corresponding numerical instability properties have been shown in Fig. 7d, for which one notices a maximum value of $|G_1||M|$ corresponding to $kh = 2.502$ at R, a value which is higher than that was noted for AB2–OUCS3 scheme. Apart from higher wavenumber of the response

wave–packet with VTSPC method, the growth rate is also significantly higher, as Fig. 7b shows the response only after $51\Delta t$. Also, the constituent wavenumbers of the response wave–packet are so close together that the wave–packet obtained is also very wide. The Fourier transform of all the 51 solutions at each time step is shown in Fig. 7c.

In Fig. 8 we display the solution of Eq. (1) for the case of VTSPC method used with Lele's 10^{th}–order spatial discretization scheme, along with an eighth–order compact filter described in [8]. This filter was needed to numerically stabilize the basic method. In this case, the filter being central, is a real function of kh. Hence, application of the filter with the basic numerical method will not change the dispersion properties, as explained in [18]. However, $|G_1||M|$ and $|G_2||N|$ contours will change radically for higher kh, as shown in Fig. 8c. Qualitatively, one observes the response field to display a similar behavior, as that is shown in Fig. 7. In this case also, the input signal propagation is studied for $N_c = 0.6$ and $k_0h = 0.1723782$.

As compared to Fig. 7, effects of filtering is clearly observed in bringing out a qualitatively different error propagation phenomenon. Unlike the case of Fig. 7 (with response stationary, due to corresponding numerical group velocity being zero), in this case the dispersion property remains the same, while maximum error growth is seen to occur for a lower value of $kh = 1.774$, for which the group velocity is non-zero. Thus, the response field represents propagating wave–packets, with constituents of every wave–packet having very large resolved wavenumbers. It is also interesting to note that such wave–packets mutually interact and create secondary wave–packets, where each of the constituents have larger distance from each other. Thus, the effect of filtering is to transform the numerical absolute instability to numerical convective instability [6], a distinctly interesting positive feature of using central filter that removes the absolute instability. In this methods, one may not see explosive growth at a fixed location for the filtered case, as opposed to the basic method which will be centered at a fixed location and amplitude continuously growing in time. This must have motivated the authors in [7, 8] to use filter in the first place, along with lower value of N_c, for which the focusing would be delayed further.

4. Focusing of error for AB2-Scheme in Solving Navier–Stokes Equation

Next we discuss about AB2 time integration scheme to show how focusing is caused for the solution of Navier–Stokes equation. For this purpose, we adopt the flow inside a square LDC to show this absolute instability. For post–Hopf bifurcation Reynolds numbers, this flow is known to be unsteady and a unique triangular gyrating vortex is formed in the core of the cavity in a transient state [23, 28, 29]. In these references, high accuracy combined compact difference (CCD) scheme [23, 28] have been used for spatial discretization and two–time level, four-stage, fourth-order Runge–Kutta (RK4) scheme has been used for time advancement. In the present results, the RK4 scheme is replaced by second–order AB2 scheme and we mark out a region for a chosen CFL number, where absolute instability is noted. Thus, this exercise extends the demonstration of focusing phenomenon for Navier–Stokes equation, which has been shown in the previous section, in the linear framework for both explicit central spatial schemes and two Hermitian spatial discretization schemes.

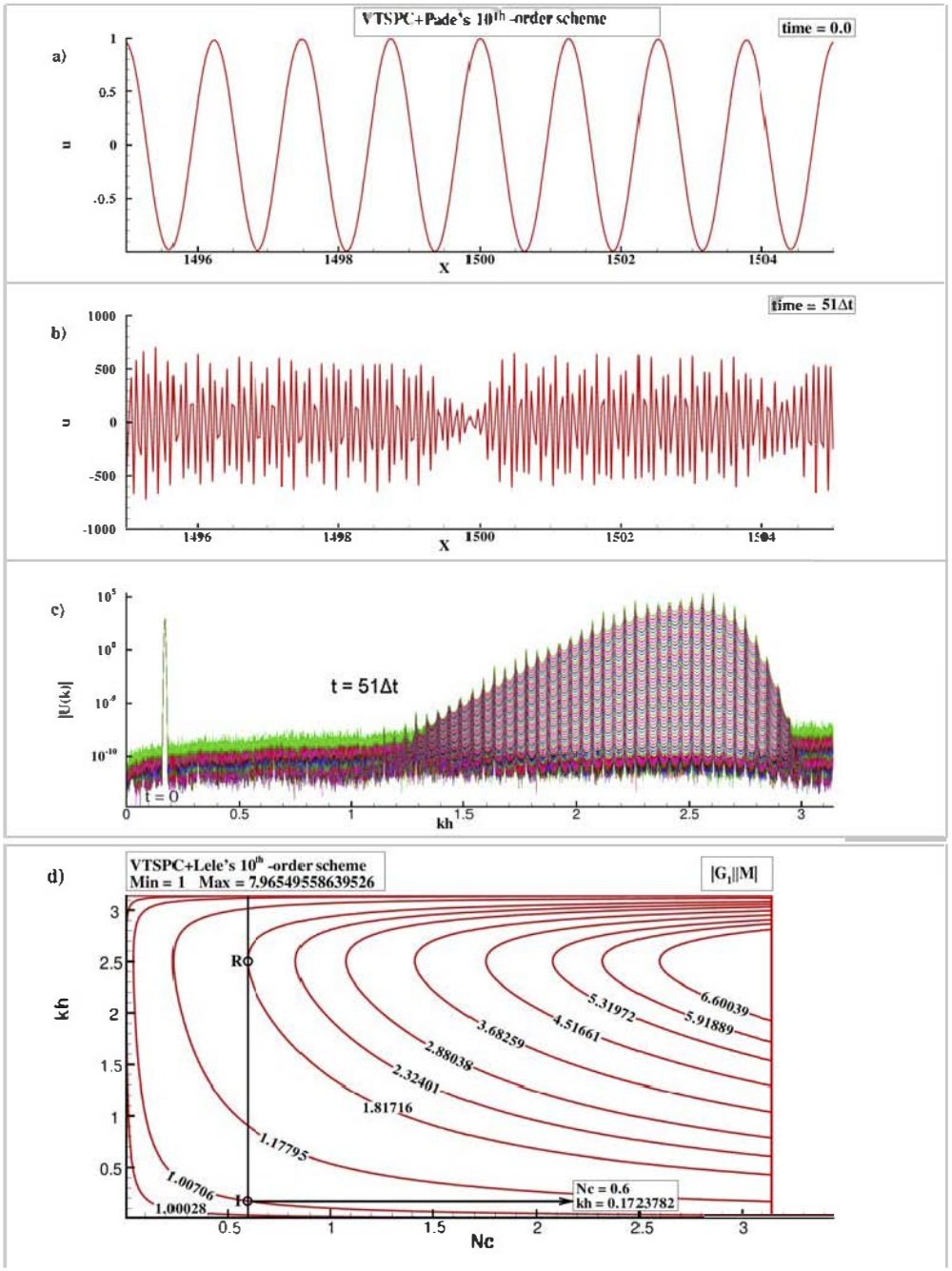

Figure 7: Demonstration of focusing of numerical solution for Eq. (1) by VTSPC method along with Lele's 10^{th}–order spatial scheme for initial solution having $k_0h = 0.1723782$ and time step given by $N_c = 0.6$; (a) Initial signal shown centered at $x_0 = 1500$; (b) Response signal at $t = 51\Delta t$, with focusing affecting the entire domain; (c) Demonstration of focusing by plotting time evolution of $U(k)$ as a function of kh; (d) Numerical amplification rate of the physical mode for this method used to solve Eq. (1).

In Fig. 9, vorticity contours are shown inside the LDC computed for $Re = 10,000$ at $t = 40.0245$ with a CFL number of $N_c = 0.27136$. The solution eventually blows up at a location

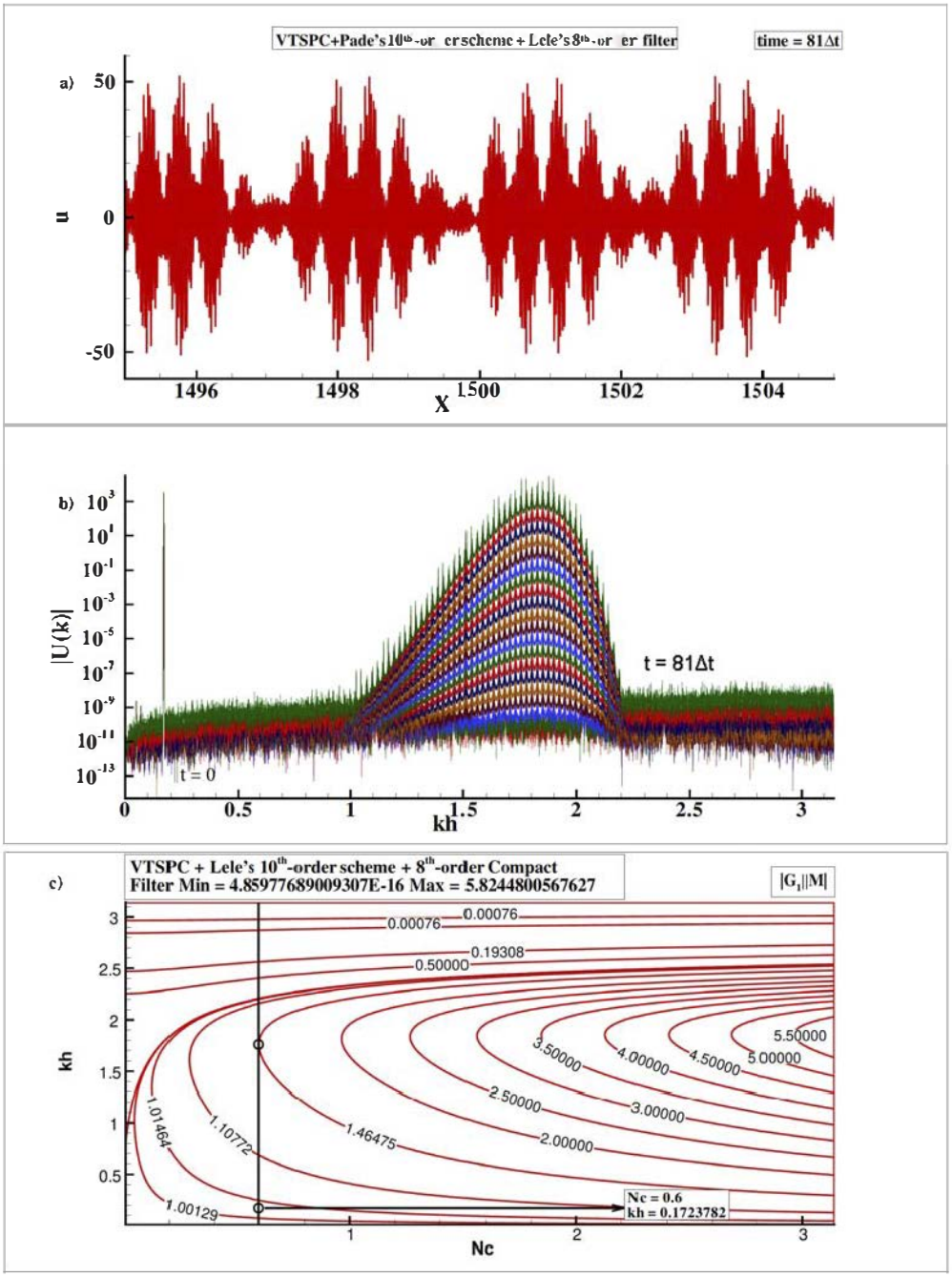

Figure 8: Solution of Eq. (1) by VTSPC method with Lele's 10^{th}–order spatial scheme along with 8^{th}–order central Padé filter computed for $k_0h = 0.1723782$ and $N_c = 0.6$ as initial solution; (a) Response signal shown at $t = 81\Delta t$; (b) Demonstration of maximum growth of signal as a function of kh, with time as parameter; (c) The numerical amplification rate of the VTSPC and Lele's 10^{th}–order spatial scheme used with 8^{th}–order Padé filter.

at $x = 0.8329$ and $y = 0.1812$, immediately after $t = 40.66$. This point is at the intersection of the line shown in this figure as the P_1–line and the Q_1–line. To establish that the solution breakdown is indeed due to temporal growth of error (with virtually negligible convection

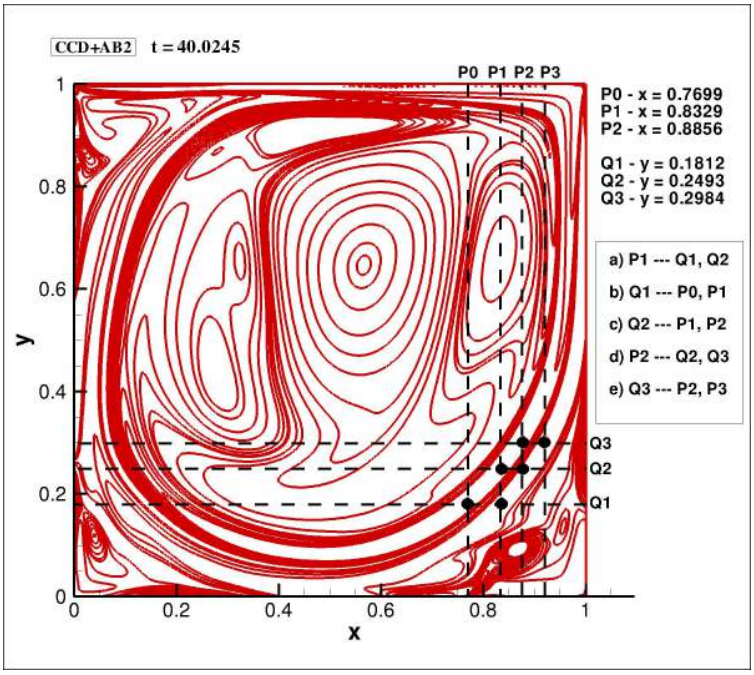

Figure 9: Vorticity contours for LDC problem at the indicated time for Re = 10,000 using CCD–AB2 for space-time discretization. The intersection points of the horizontal and vertical lines are the locations of absolute instability, which are the focusing points of errors.

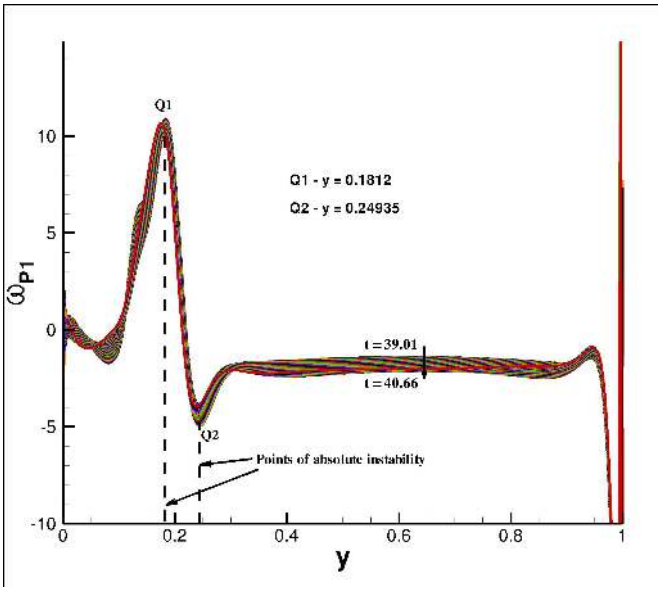

Figure 10a: Vorticity variation along the vertical P_1–line and primary absolute instability is noticed at Q_1 ($y = 0.1812$).

of the error at this point), we track the solution as a function of time for the horizontal and vertical lines shown by dashed lines in Fig. 9.

In Fig. 10a, the vorticity solution along the vertical P_1–line is plotted during the time interval

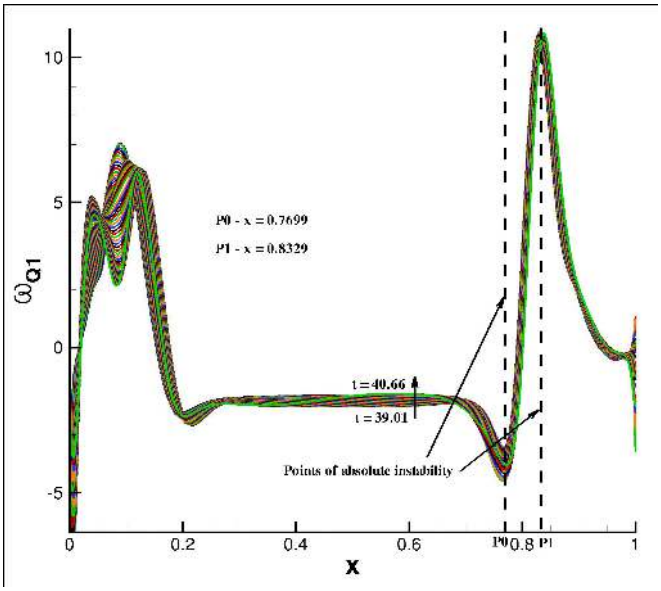

Figure 10b: Vorticity variation along the horizontal Q_1–line and primary absolute instability is noticed at P_1 ($x = 0.8329$).

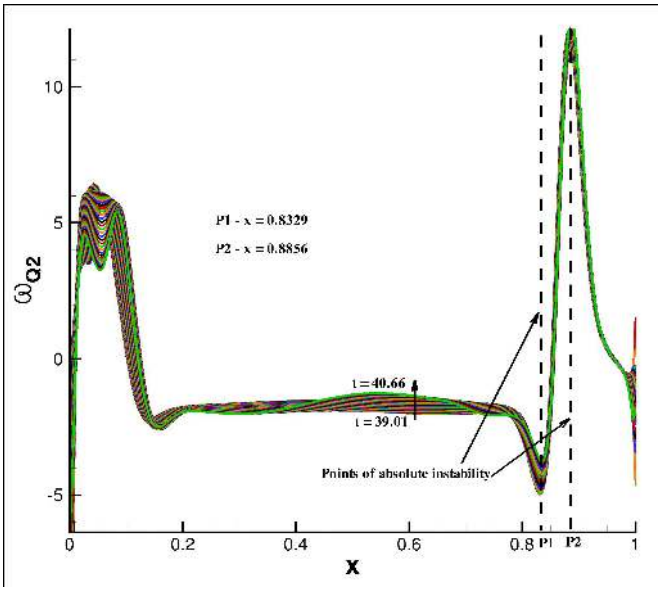

Figure 10c: Vorticity variation along the horizontal Q_2–line and primary absolute instability is noticed at P_2 ($x = 0.8856$).

$t = 39.01$ to 40.66. One notices temporal growth of the solution at the intersection point with the horizontal Q_1–line and at an additional secondary site at the intersection of horizontal Q_2–line, where the solution grows almost monotonically with time, but with lower magnitude. In the same way, the computed vorticity plotted in Fig. 10b, along the horizontal Q_1–line, shows the major temporal growth corresponding to the intersection point of vertical P_1–line and a secondary site at the intersection of the horizontal Q_1–line with the vertical P_0–line passing through $x = 0.7699$. In Fig. 10c, we plot the vorticity as a function of x along

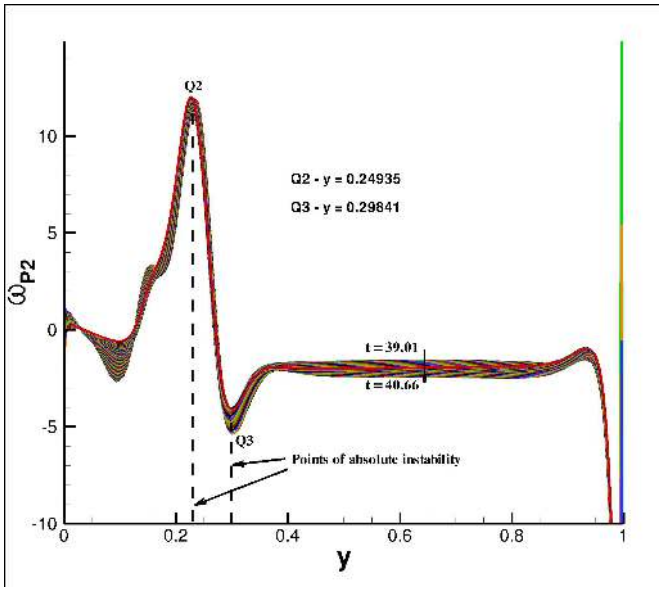

Figure 10d: Vorticity variation along the vertical P_2-line and primary absolute instability is noticed at Q_2 ($y = 0.24935$).

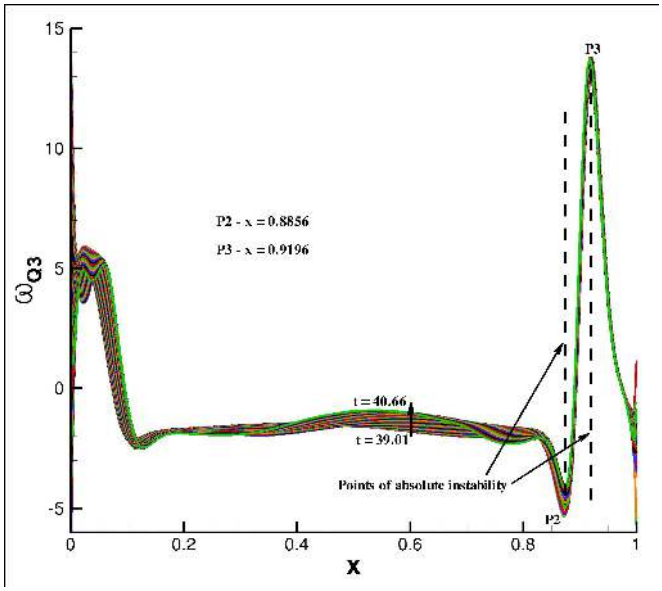

Figure 10e: Vorticity variation along the horizontal Q_3–line and primary absolute instability is noticed at P_3 ($x = 0.9196$).

Q_2–line for the indicated time range and one notices the primary growth site to be at the intersection with vertical P_2–line, while the secondary temporal growth is noted with the intersection point along P_1–line. In Fig. 10d, we plot the vorticity along the vertical P_2–line, which similarly identifies the primary absolute instability, where it intersects with the horizontal Q_2–line. The secondary site is at the confluence with the Q_3–line. In Fig. 10e, the vorticity along the horizontal line passing through Q_3 is plotted and we note, the primary instability to occur at P_3, while a secondary absolute instability is noted for P_2–line.

While discussing the flow field in Fig. 9, we have mentioned above that the solution blows up spectacularly immediately after $t = 40.66$. This is further shown with the time–snapshots of vorticity contours leading to solution blow up in the top four frames of Fig. 11. In each of the frames, the maximum and minimum values of vorticity are marked and thereby one can notice that the solution grows very rapidly from $t = 40.62$ to 40.66. This is exemplified by tracing the vorticity at the point ($x = 0.8329,\ y = 0.1812$) as a function of time, shown in the bottom frame of Fig. 11. The explosive growth of the solution is clearly evident from the exponential temporal growth leading to solution breakdown by numerical absolute instability caused by focusing.

Thus, it is evident that the maximum growth of vorticity is noted primarily at (0.8329, 0.1812) which migrates to (0.8856, 0.2493). This sequence of error growth eventually contaminates the entire flow field which exhibits error growth with time and complete solution breakdown occurs immediately after $t = 40.66$, which follows the frames shown in Figs. 9 and 11.

5. Conclusions

Global Spectral Analysis (GSA) [18] of various spatial schemes in conjunction with the AB2 method is reported to elucidate the numerical properties of the physical and numerical modes shown for signal propagation in [26]. AB2 method used with CD2 and CD4 schemes display numerical amplification along with dispersion as a major source of error. For both the spatial schemes, one observes q–waves [19], along with a specific kh for every N_c where the group velocity is zero and the numerical amplification is maximum. As the maximum numerical instability of the combined method increases with N_c, its evidence is shown in Fig. 1, for AB2–CD2 method for $N_c = 0.2$. This figure indicates the basic signature of focusing at its early times. However, such focusing completely depends upon the numerical property and no single rule of thumb could be provided. For the EXT2–CD2 method, which showed the most accurate solution for the benchmark computational aeroacoustic problem [9] for $N_c = 0.1$ and $k_0h = 0.3$ in [26], no such focusing could be noted for $N_c = 0.2$ in the results shown in Fig. 3 explained with the properties shown in Figs. 2a and 2b.

The focusing phenomenon, wherein a violent instability appears in short duration of computing time and causes solution to blow up eventually, at a location in k-space, is shown for AB2 method. The solutions of the 1D convection equation with AB2–CD2, AB2–CD4, AB2–OUCS3 and VTSPC–Lele combination are analyzed and shown in Figs. 4 to 7. Focusing is associated with localization in k-space, while signal forms wave–packets everywhere in the physical space, with the response remaining frozen in space and amplitude growing continuously in time, an attribute of numerical absolute instability [6]. The Fourier transforms of the wave–packet show focusing to be centered around $kh = 1.565, 1.8, 2.4, 2.502$ for AB2–CD2, AB2–CD4, AB2–OUCS3, VTSPC–Lele (without filter), respectively. For VTSPC-Lele scheme (with filter) one notices maximum growth of convecting error around $kh = 1.774$. Of specific interest is the finding of the present study that focusing is caused only when a combined space-time integration method displays a value of kh for which the physical or numerical mode display zero numerical group velocity and the numerical amplification factor

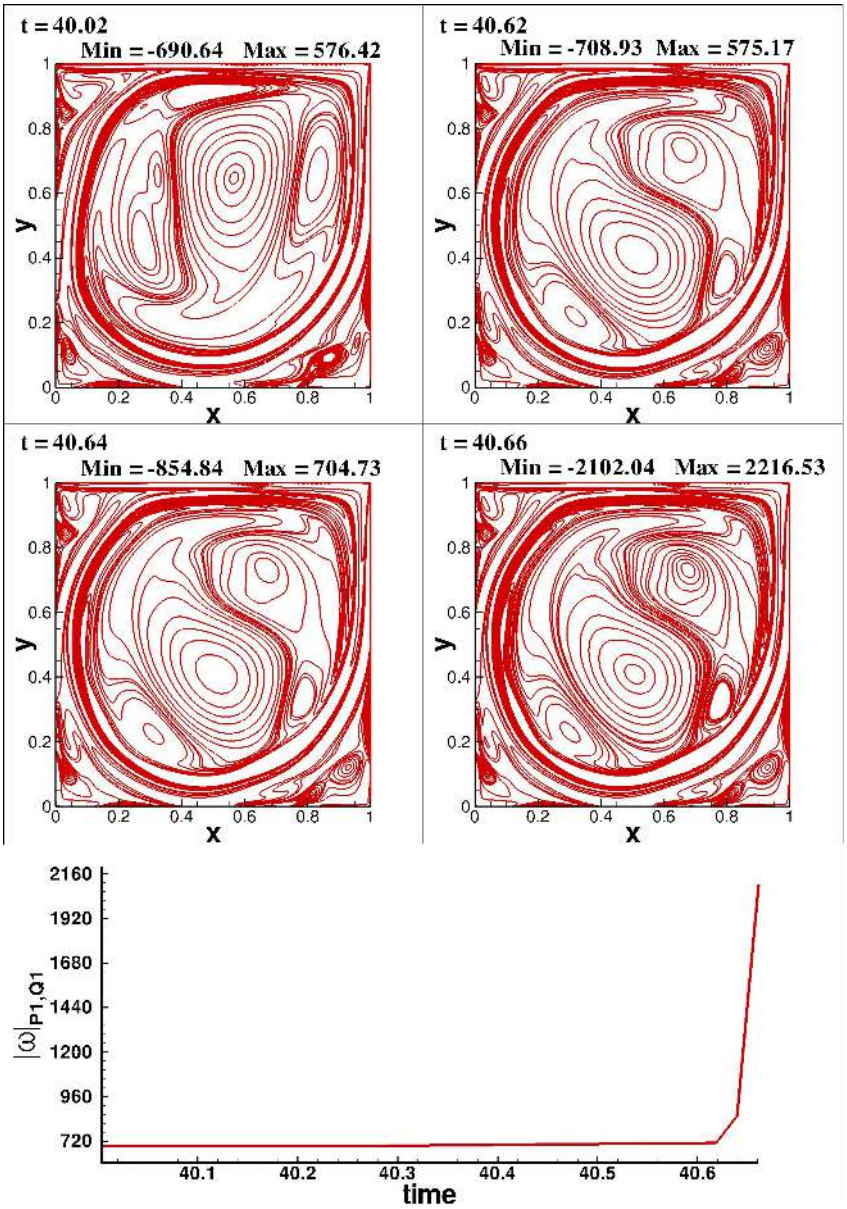

Figure 11: Vorticity contours are shown in the top four frames, as obtained by solution of Navier–Stokes equation, for the square LDC problem at the indicated times for Re = 10,000 using CCD–AB2 method. In the bottom frame, time history of vorticity at the point ($x = 0.8329,\ y = 0.1812$) is shown leading to solution breakdown by focusing.

for that combination of kh and N_c also indicates numerical instability, eventually leading to numerical absolute instability [6]. Such absolute instability can be avoided by the use of symmetric Padé filter, which makes the maximum growth rate for a particular N_c to have non-zero group velocity, thereby avoiding the possibility of focusing. However, such convective instability will also make such results of no physical relevance. This is clearly shown from the solution of Navier–Stokes equation by CCD–AB2 method for flow inside a square lid driven cavity for a Reynolds number of 10,000. When CCD method of spatial discretization was used with RK4 time integration method [23, 28], one noticed polygonal

core vortex forming transiently and the flow can be computed indefinitely. Such polygonal core vortex forms due to Hopf–bifurcations, as explained with the help of proper orthogonal decomposition in [29]. However for CCD–AB2 method, the solution breaks down due to numerical absolute instability by focusing, as explained from the solution of 1D convection equation in [26] elucidated in the numerical property charts.

References

[1] Bashforth, F., and Adams, J.C. (1883). *An attempt to test the theories of capillary action by computing the theoretical and measured forms of drops of fluid.* Cambridge Univ. Press, UK.

[2] Bhumkar, Y.G., Rajpoot, M.K., and Sengupta, T.K. (2011). A linear focusing mechanism for dispersive and non-dispersive wave problems. *J. Comput. Phys.*, **230**, 1652–1675.

[3] Briggs, W.L., Newell, A.C., and Sarie, T. (1983). Focusing: A mechanism for instability. *J. Comput. Phys.*, **51**, 83–106.

[4] Brillouin, L. (1960). *Wave Propagation and Group Velocity.* Academic Press-New York, USA.

[5] Charney, J.G. Fjörtoft, R., and Neumann, J.V. (1950). Numerical integration of the barotropic vorticity equation. *Tellus*, **2**, 237–254.

[6] Cossu C., and Loiseleux, T. (1998). On the convective and absolute nature of instabilities in finite difference numerical simulations of open flows. *J. Comput. Phys.*, **144**(1), 98–108.

[7] Cabot, W.H., and Cook, A.W. (2006). Reynolds number effects on Rayleigh-Taylor instability with implications for type 1a supernovae. *Nature*, **2**, 562–568.

[8] Cook, A.W., Cabot, W., and Miller, P.L. (2004). The mixing transition in Rayleigh-Taylor instability. *J. Fluid Mech.*, **511**, 333–362.

[9] Dahl, M., Envia, E., Hu, D., and Tam, C. (2004). *Problem 1 of Category 1 in Fourth Computational Aeroacoustics (CAA) Benchmark Problems.* NASA/CP-2004-212954.

[10] Durran, D. R. (1999). *Numerical Methods for Wave Equations in Geophysical Fluid Dynamics*, Springer Verlag-New York, USA.

[11] Fornberg, B. (1973). On the instability of Leap-Frog and Crank-Nicolson approximations of a nonlinear partial differential equation. *Math. Comput.*, **27**(121), 45–57.

[12] Kawamura, T., Takami, H., and Kuwahara, K. (1985) A new higher order upwind scheme for incompressible Navier–Stokes equation. *Fluid Dyn. Res.*, **1**, 145–162.

[13] Kim, J., and Moin, P. (1973). Application of fractional step method to incompressible Navier–Stokes equation. *J. Comput. Phys.*, **58**, 308–323.

[14] Kim, J., Moin, P., and Moser, R.D. (1987). Turbulence statistics in fully developed channel flow at low Reynolds number. *J. Fluid Mech.*, **177**, 133–166.

[15] Kreiss, H., and Oliger, J. (1972). Comparison of accurate methods for the integration of hyperbolic equations. *Tellus*, **24**, 199–215.

[16] Lomax, H., Pulliam, T.H., and Zingg, D.W. (2002). *Fundamentals of Computational Fluid Dynamics*, Springer Verlag-Berlin, Germany.

[17] Newell, A.C. (1977). Finite amplitude instabilities of partial difference equations. *SIAM J. Appl. Math.*, **32**(1), 133–160.

[18] Sengupta, T.K. (2013). *High Accuracy Computing Methods: Fluid Flows and Wave Phenomenon*. Cambridge Univ. Press, USA.

[19] Sengupta, T.K., Bhumkar, Y.G., Rajpoot, M.K., Suman, V.K., and Saurabh, S. (2012). Spurious waves in discrete computations of wave phenomena and flow problems. *App. Math. Comput.*, **218**(18), 9035–9065.

[20] Sengupta, T.K., and Dipankar, A. (2004). A comparative study of time advancement methods for solving Navier-Stokes equation. *J. Sci. Comp.*, **21**, 225–250.

[21] Sengupta, T.K., Dipankar, A., and Sagaut, P. (2007). Error dynamics: Beyond von Neumann analysis. *J. Comput. Phys.*, **226**, 1211–1218.

[22] Sengupta, T.K., Ganeriwal, G., and De, S. (2003). Analysis of central and upwind compact schemes. *J. Comput. Phys.*, **192**, 677–694.

[23] Sengupta, T.K., Lakshmanan, V., and Vijay, V.V.S.N. (2009). A new combined stable and dispersion relation preserving compact scheme for non-periodic problems. *J. Comput. Phys.*, **228**, 3048–3071.

[24] Sengupta, T.K., Sathyanarayanan, V.K., Sriramakrishnan, M., and Mulloth, A. (2015). Role of time integration in computing transitional flows caused by wall excitation. *J. Sci. Comput.*, **65** 224-248.

[25] Sengupta, T. K. and Sengupta, R. (1994) Flow past an impulsively started circular cylinder at high Reynolds number. *Comput. Mechanics*, **14(4)**, 298-310.

[26] Sengupta, T.K., Sengupta, A., and Saurabh, K. (2017). *Global spectral analysis of multi-level time integration schemes. Part I: Numerical properties for error analysis. Applied Mathematics and Computation*, **304**, 41–57.

[27] Sengupta, T.K., Sircar, S.K., and Dipankar, A. (2006). High accuracy schemes for DNS and acoustics. *J. Sci. Comput.*, **26**, 151–193.

[28] Sengupta, T.K., Vijay, V.V.S.N., and Bhaumik, S. (2009a). Further improvement and analysis of CCD scheme: Dissipation discretization and de-aliasing properties. *J. Comput. Phys.*, **228**, 61506168.

[29] Sengupta, T.K., Vijay, V.V.S.N., and Singh, N. (2011). Universal instability modes in internal and external flows. *Comput. Fluids*, **40**, 221–235.

[30] Sloan D.M., and Mitchell, A.R. (1986). On nonlinear instabilities in Leap-Frog finite difference schemes. *J. Comput. Phys.*, **67**, 372–395.

[31] Trefethen, L.N. (1982). Group velocity in finite difference schemes. *SIAM Rev.*, **24**(2), 113–136.

[32] Vichnevetsky, R., and Bowles, J.B. (1982). Fourier Analysis of Numerical Approximations of Hyperbolic Equations. *SIAM Stud. Appl. Math.* 5, SIAM-Philadelphia, USA.

[33] Zingg, D.W. (2000). Comparison of high-accuracy finite-difference schemes for linear wave propagation. *SIAM J. Sci. Comput.*, **22**(2), 476–502.